Nanoscale

Accepted Manuscript

Volume 10
Number 4
28 January 2018
Pages 1549-2172

Nanoscale

rsc.li/nanoscale

ISSN 2040-3372

PAPER
Shuping Xu, Chongyang Liang et al.
Organelle-targeting surface-enhanced Raman scattering
(SERS) nanosensors for subcellular pH sensing

ROYAL SOCIETY
OF CHEMISTRY

NCNST

ROYAL SOCIETY
OF CHEMISTRY

rsc.li/nanoscale

Journal Name

ARTICLE

Radiative cooling of solar cells: opto-electro-thermal physics and modeling

Yidan An, [† a,b] Chunxiang Sheng [† a,b] and Xiaofeng Li * [a,b]

Passive radiative cooling technology has attracted intensive attention with addressing the potential application in effectively cooling the photovoltaic and related systems. Here, we realize a comprehensive multi-dimensional & multiphysical opto-electro-thermal (OET) modeling, which is used to design a silicon-based radiative cooling solar cell (SC). Our study simultaneously takes into account the coupled effects of radiative cooling characteristics, carrier thermodynamic and electrodynamic behaviors of SC in spatial and frequency domains. Based on comprehensive photonic design, we present a radiative cooler with a near-ideal spectral selectivity from sunlight to infrared band. The fundamental OET physical mechanisms and temperature effect on the performance of SC are explored. A comparable study on the performance parameters of the SCs with and without the radiative cooler is given, which shows that the SC temprature can be reduced by over 10 °C and the absolute power conversion efficiency (PCE) can be increased by 0.45% with employing the photonic radiative cooler. Our OET study provides a readily way to explore the comprehensive OET physics in photovoltaic systems.

1 Introduction

The detailed balance analysis by thermodynamic principle has indicated that a single-junction solar cell (SC) has a theoretical upper limit of the power conversion efficiency (PCE) of around 33% under the AM 1.5 solar illumination.[1] This means that a significant portion of solar energy absorbed by the SC has actually been converted into the unwanted heat (rather than the useful electricity) via different channels, which greatly raises the operating temperature and degrades the stability of the SCs.[2−4] At present, the PCEs in lab of typical SCs based on Si, GaAs or perovskite have already surpassed 23% (or even approaching 30%) by dint of advanced photon managements and carrier transport optimizations.[5−7] However, the typical operating temperature of single-junction photovoltaic (PV) system can reach around 50−55 °C (which is even much higher for concentrated SCs) in outdoor condition.[8, 9] The thermal effect is detrimental for achieving reliable high-efficiency SCs.[10, 11] For example, for the mono-crystalline silicon (c-Si) PV array, every 1 °C rise in temperature leads to a relative efficiency decline of ~ 0.45% and the exponentially increased aging rate[10, 11] Therefore, the strategies that are capable of effectively cooling the PV systems are highly desired.

The conventional cooling strategies include the heat pipe,[12] forced air flow circulation,[13] water cooling,[14] thermoelectric cooling, phase-change materials, etc.[15, 16] However, most of them need extra energy input, which increases the system complexity as well as degrades the energy-utilization efficiency. In recent years, the radiative cooling mechanism has attracted tremendous interests since it only relies on the thermal emission of the designed radiative cooler to lower the temperature of the PV system without any external energy inputs.[17−23] Currently, most literatures focus on the fabrication of radiative coolers and the evaluation of the cooling effect.[18, 22] For example, Lu et al. deposited the textured SiO_2 on the Si PV module to enable the PCE enhancement over 0.5%;[17] the temperature decline of 13 °C was observed in experiment through integrating the designed silica (SiO_2) photonic crystal on top of a doped silicon wafer.[18] On the other hand, theoretical studies mainly concentrate on designing a high-performance radiative cooler and showing its spectral selectivity and cooling effect, but those are based on the simplified one-dimensional optical-thermal or opto-electro-thermal (OET) model.[9, 19−22] For example, by designing a SiO_2 pyramid structure, Zhu et al. theoretically demonstrated that the operating temperature of SC can be reduced by ~ 18.3 °C based on an optical-thermal model;[19] Li et al. demonstrated that the temperature of encapsulated solar panels can be reduced by over 5.7 °C after using multilayer photonic design;[21] Sun et al. calculated the radiation power and temperature decrease of a SiO_2 bulk material by an analytical OET method.[9]

In these studies, the multilayer or more complicated photonic crystal structures were extensively used; moreover, the infrared thermal radiation of the designed radiative cooler was considered, but the filtering function at the sunlight band of 1.1−4 µm can be further improved.[17−20, 22, 23] Thus, designing the radiative cooler with easy fabrication and high-performance spectral selectivity within the range from sunlight to infrared band is highly necessary but remains to be challenging. This is because the precise control of the spectral response of the radiative cooling system for SC application relies on a thorough understanding on the intrinsic optical, electrical, and thermodynamic characteristics; moreover, the related fundamental physics have to be examined in both macroscopic

a. School of Optoelectronic Science and Engineering & Collaborative Innovation Center of Suzhou Nano Science and Technology, Soochow University, Suzhou 215006, China.
b. Key Lab of Advanced Optical Manufacturing Technologies of Jiangsu Province & Key Lab of Modern Optical Technologies of Education Ministry of China, Soochow University, Suzhou 215006, China.
*E-mail: xfli@suda.edu.cn.
† These authors contributed equally to this work.

(e.g., the heat caused by sunlight, thermal radiation of atmosphere and radiative cooler, and non-radiative heat exchange process) and microscopic (e.g., carrier thermodynamics and carrier transports) levels. All these strongly desire a comprehensive study on the coupled OET effects. Such an OET study must address the very detailed multi-domain and multi-scale OET responses, including electromagnetic absorption, electron-hole behaviors in generation/transportation/recombination/collection processes, and heat generation/transport/radiation in multi-spatial and frequency (or time) domains.

In this work, we report a comprehensive multi-dimensional OET modeling of the radiative cooling SC system in order to deeply uncover its intrisic multiscale physics as well as guide the design of high-performance radiative cooler for SCs. The simulation is implemented by addressing the electromagnetic response, carrier transport dynamics (generation/recombination/transportation/ collection), microscopic carrier thermodynamic processes (thermalization/joule/recombination/Peltier heat), as well as the macroscopic thermal conduction, radiation and diffusion processes (e.g., sunlight absorpiton, non-radiative heat exchange, atmosphere radiation, cooler radiation, etc.) in the radiative cooling system of SC. First, the fundamental physical mechanisms of the passive radiative cooling and carrier thermodynamic/electrondynamic principles in SC are analyzed. We then design a high-performance radiative cooler through photonic method. Next, we present a detailed analysis of macroscopic energy conversion process in radiative cooling SC system and quantitatively analyze the carrier thermo/electro-dynamic behaviors under the forward bias. Finally, the thermal effect on the optoelectronic performance of the SC and the influence of weather condition on the radiative cooler are explored. Such a comprehensive multi-dimensional OET model provides an useful platform for deeply uncovering the fundamental OET science as well as accurately predicting the performance of OET devices from both microcospic and macrocospic perspectives.

2 Methods

2.1 OET physics and modeling of radiative cooling SCs

Based on the optoelectronic model of SCs and the pioneering work of OET multiphysics simulation for GaAs SCs,[4, 23−28] the OET simulation of radiative cooling SC system can be implemented by simultaneously addressing the optical, electrical and thermal processes by finite-element method in the platform of COMSOL multiphysics. Optically, the light reflectivity (R), transitivity (T) and emissivity (E) are obtained by solving the Maxwell's equations. Electrically, the carrier generation-recombination-transportation-collection behaviors, driven by the built-in electric field, carrier concentration gradient, temperature gradient, etc., are accurately treated. Thermodynamically, the macroscopic heat generation and dissipation processes (including the solar illumination, thermal emission of radiative cooler and atmosphere, and non-radiation heat exchange) are all considered through the steady-state heat diffusion equation; from the microscopic perspective, the carrier thermodynamic behaviors (including thermalization, Joule heat, recombination

heat, and Peltier heat) are taken into consideration by solving the carrier thermodynamic equation.

Looking inside the macroscopic thermodynamics, when the radiative cooling system of SC is exposed to the clear sky, there are four heat exchange processes, i.e., 1) absorption of the solar irradiance, 2) thermal radiation of the radiative cooler, 3) absorption of the thermal radiation from atmosphere, and 4) convection and conduction heat exchanges between the radiative cooling system and the ambient air. To such a radiative cooler with area A and temperature T, the thermal radiation power of the radiative cooler (P_{rad}) can be given by:[29]

$$P_{rad}(T) = A \int d\Omega \cos\theta \int_0^\infty d\lambda I_{BB}(T,\lambda)\varepsilon(\lambda,\theta) \tag{1}$$

where $\int d\Omega = 2\pi \int_0^{\pi/2} d\theta \sin\theta$ is the angular integral over the hemisphere, $I_{BB}(T,\lambda) = \dfrac{2hc^2}{\lambda^5} \dfrac{1}{e^{hc/(\lambda k_B T)} - 1}$ the spectral radiance of a blackbody at the temperature T, $\varepsilon(\lambda,\theta)$ the directional spectral emissivity, h the Planck's constant, k_B the Boltzmann constant, c the light speed, and λ the thermal radiation wavelength. By integrating the spectral irradiance, the total radiation power density can be obtained according to the Stefan-Boltzmann law:

$$P_{rad}(T) = A\bar\varepsilon\sigma T^4 \tag{2}$$

where σ is the Stefan-Boltzmann constant and $\bar\varepsilon = \int_0^\infty d\lambda I_{BB} \int_0^{\pi/2} d(\sin^2\theta)\varepsilon(\theta,\lambda) \big/ \int_0^\infty d\lambda I_{BB}$ the average emissivity of the radiative cooler. The absorbed radiation power from the atmosphere can be defined as: [29]

$$P_{atm}(T_{amb}) = A \int d\Omega \cos\theta \int_0^\infty d\lambda I_{BB}(T_{amb},\lambda)\varepsilon(\lambda,\theta)\varepsilon_{atm}(\lambda,\theta) \tag{3}$$

where T_{amb} is the ambient temperature, $\varepsilon_{atm}(\lambda,\theta) = 1 - t(\lambda)^{1/\cos\theta}$ the angle-dependent emissivity of the atmosphere,[30] and $t(\lambda)$ the atmosphere transmittance in the zenith direction.

The solar power absorbed by the radiative cooling system is written as:[29]

$$P_{sun} = A \int d\lambda \varepsilon(\lambda,\theta_{sun}) I_{AM1.5}(\lambda) \tag{4}$$

where $I_{AM1.5}$ is the standard AM 1.5 solar spectrum. The top/bottom non-radiative heat exchange powers between the radiative cooling system and ambient air (i.e., the convection and conduction heat exchange processes) is

$$P_{non}^{T/B}(T, T_{amb}) = Ah_{top/bottom}(T - T_{amb}) \tag{5}$$

where $h_{top/bottom}$ is the top/bottom surface non-radiative heat exchange coefficient of radiative cooling system representing the ability of the non-radiative heat dissipation, which is weighed by the wind speed for the typical environment situation.[31]

For SCs, as we have indicated that a significant portion of the absorbed solar energy is converted into heat rather than the useful electricity. From carrier thermodynamic perspective, when a photon is absorbed by the SC, the energy of the photogenerated hot carrier can be dissipated by three kinds of heat channels in bulk: 1) thermalization (P_{th}) arising from the thermal relaxation process of the generated hot carriers, 2) Joule heat (P_{Joule}) caused by the carrier movements with the presence of the built-in electric field, i.e., the self-heating effect, and 3) bulk recombination heat (P_{rec}^{bulk}). Simultaneously, the hot-carrier energy is also consumed by two kinds of heat mechanisms at the surface of SC, i.e., 1) surface recombination heat (P_{rec}^{surf}) due to the minority carrier recombination process

and 2) Peltier heat ($P_{Peltier}^{n/p}$) arising from the electron (hole) energy relaxation process from the conduction (valence) band to the corresponding quasi-Fermi level (when the electron or hole is collected by the electrode). The energy dissipation (also heat generation) processes in SC can be defined by:[4]

$$P_{th}(x,y,z) = \int (hv - E_g) \cdot g(x,y,z,\lambda) \qquad (6)$$

$$P_{Joule}(x,y,z) = F \cdot J \qquad (7)$$

$$P_{rec}^{bulk}(x,y,z) = E_g \cdot U_{bulk}(x,y,z) \qquad (8)$$

$$P_{rec}^{surf}(x,y,z) = E_g \cdot U_{surf}(x,y) \qquad (9)$$

$$P_{Peltier}^{n/p}(x,y) = \left| (E_{c/v} - E_{fn/fp}) \right| \cdot J \qquad (10)$$

where $hv - E_g$ is the excess photon energy, $g(x,y,z,\lambda)$ the carrier generation rate, J the current density, F the built-in electric field, U_{bulk} the bulk recombination rate (Shockley-Read-Hall and Auger recombination), U_{surf} the surface recombination rate, $E_{c/v}$ the conduction/valance energy level, and $E_{fn/fp}$ the electron/hole quasi-Fermi level.

For the SC, the carrier thermodynamics are closely related to the carrier transport behaviors. Therefore, the coupled carrier thermodynamic and electrodynamic behaviors are included in our OET model:[4]

$$\nabla^2 \Phi = \frac{q}{\varepsilon_0 \varepsilon_r}(n - p - C) \qquad (11)$$

$$\nabla \cdot \left[-D_n \nabla n + n\mu_n \left(\nabla \Phi + \frac{\nabla \chi}{q} + \frac{k_B T}{q} \nabla \ln N_c \right) - nD_{th}^n \nabla T \right] \\ = G(x,y,z) - U \qquad (12)$$

$$\nabla \cdot \left[-D_p \nabla p - p\mu_p \left(\nabla \Phi + \frac{\nabla \chi}{q} + \frac{\nabla E_g}{q} - \frac{k_B T}{q} \nabla \ln N_V \right) - pD_{th}^p \nabla T \right] \\ = G(x,y,z) - U \qquad (13)$$

$$\nabla \cdot (-k\nabla T) = H \qquad (14)$$

where ε_r is the material permittivity, n (p) the electron (hole) concentration, Φ the electrostatic potential, D_n (D_p) the electron (hole) diffusion coefficient, D_{th}^n (D_{th}^p) the thermal diffusion coefficient for electron (hole), N_c (N_v) the effective conduction (valence) band density of states, μ_n (μ_p) the electron (hole) mobility, U the total bulk recombination, q the electron charge, C the impurity concentration, and H the net heat source generated in the SC under steady state.

In our OET model, the non-radiative heat exchange, surface recombination heat and Peltier heat are considered as the boundary heat sources, i.e., the boundary conditions; the rest heat processes are the bulk heat resources, which rely on the heat exchange positions generated or dissipated in radiative cooling system. In this study, we concentrate on the comprehensive OET physics and simulation of radiative cooling SC system by taking the 10 μm c-Si SC as an example.

2.2 Photonic principles of radiative cooler design

The multilayer thin films and the photonic crystal structures have been widely applied for broadband spectral filtering and thermal radiation purposes, respectively.[21, 22, 29, 32-36] Thus, the spectral selectivity of the radiative cooler of SC can be easily implemented by integrating the functions of multilayer thin films and the photonic crystal structures, as shown in Fig. 1. For example, the standalone daytime radiative cooler (without considering the SC application) must simultaneously meet the following two requirements: 1) a high reflection at the whole

sunlight band and 2) a high & selective thermal emission at the atmospheric transparent window, as shown in Figs. 1(a) and 1(c). Thus, it can guarantee that the temperature of daytime radiative cooler under illumination is lower than the ambient air.[29, 32-36] Comparably, more complicated spectral selectivity has to be considered for the radiative cooler used in SCs, as shown in Figs. 1(b) and 1(d). For example, for the radiative-cooler of c-Si SC, the essential considerations include:[21] 1) at the wavelength range of 0.35−1.1 μm, the radiative cooler needs to have a maximum transmittance to allow the incident photons to completely transmit through the radiative cooler and then be absorbed by the c-Si material; 2) at the 1.1−4 μm band, the sunlight has to be completely reflected to avoid the parasitic heat absorption inside the SC; 3) by the reason that the typical operating temperature of SC is higher than the atmosphere in outdoor situation, the net outward radiative power from radiative cooler to atmosphere is beneficial for lowering the operating temperature of PV devices; hence, a broadband thermal radiation is necessary for the whole infrared range (e.g., 4−25 μm).
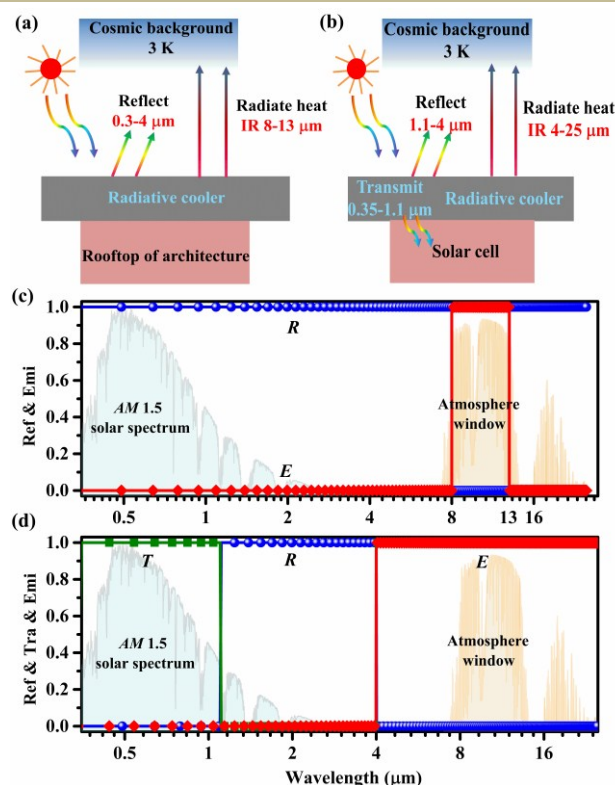

Fig.1 (a) The schematic of the designed radiative cooling system applied in the c-Si SC (left), which integrates the multilayer thin-film stack and the SiO₂ grating. The 1D multilayer stack is composed of 10 layers thin films and the structure parameters of SiO₂ grating are shown in (a). (b) The simulated transmissivity and emissivity spectra of planar and grating silica structures. (c) and (d) are the spectral selectivity of the radiative cooler under the TE incidence at sunlight and infrared bands, respectively, where the ideal spectral responses, the normalized AM 1.5 solar spectrum, and atmosphere windows are plotted for reference.

3 Results and discussion

3.1 Photonic design of radiative cooler for c-Si SCs

ARTICLE

Based on the principle above, we propose a radiative cooler for 10μm-thick thin-film c-Si SC as illustrated in Fig. 2(a), which integrates the multilayer thin-film stack and the SiO_2 grating. The SiO_2 material is selected due to its high extinction coefficient at the infrared band and high transmittance at the solar band. First, the transmissivity and emissivity of SiO_2 bulk material are shown in Fig. 2(b), where it can be observed that there are two emissivity dips respectively occur at the wavelengths of 9 and 21 μm arising from the strong phonon-polarization resonances of silica.[19] At these two wavelengths, silica has especially high extinction coefficients, revealing a strong resistance impedance mismatch between air and SiO_2 (as well as a high reflectivity from the interface).

In order to obtain a high-performance filtering function, the optimization of the thin-film stack of radiative cooler is implemented by employing the memetic algorithm, which is an optimization method for designing stacked thin film structures by combining the evolutionary algorithm and local optimization method.[32] The materials are selected from the common

materials in experiments, including magnesium fluoride (MgF_2), hafnium dioxide (HfO_2), silver (Ag), silicon carbide (SiC), silicon nitride (SiN), aluminum oxide (Al_2O_3) and silica (SiO_2).[37, 38] The corresponding sedimentary sequence and material thicknesses after optimization are listed in Table 1. The resulted SiO_2 grating configuration is shown in Fig. 2(a), which features a near unity thermal emissivity at infrared band as displayed in Fig. 2(b).

Table 1 The materals and thicknesses of the optimized 1D multilayer film stack.

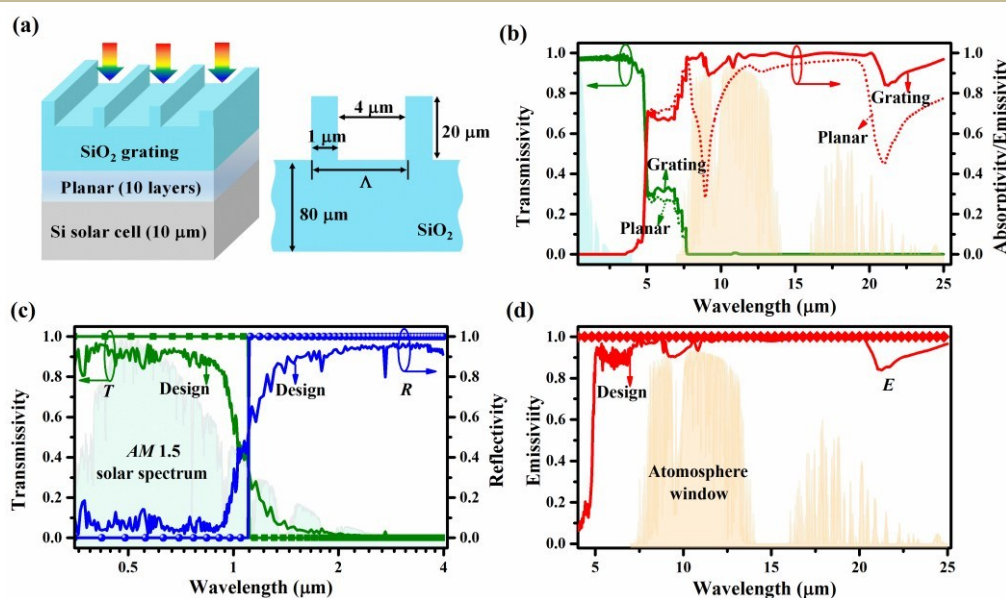| Material	Thickness (nm)	Layer sequence (from top to bottom)
MgF_2	600	1
HfO_2	39	2
Ag	8	3
HfO_2	52	4
SiO_2	40	5
SiC	23	6
Ag	8	7
SiN	21	8
Al_2O_3	147	9
SiC	42	10

Fig.2 (a) The schematic of the designed radiative cooling system applied in the c-Si SC (left), which integrates the multilayer thin-film stack and the SiO_2 grating. The 1D multilayer stack is composed of 10 layers thin films and the structure parameters of SiO_2 grating are shown in (a). (b) The simulated transmissivity and emissivity spectra of planar and grating silica structures. (c) and (d) are the spectral selectivity of the radiative cooler under the TE incidence at sunlight and infrared bands, respectively, where the ideal spectral responses, the normalized *AM* 1.5 solar spectrum, and atmosphere windows are plotted for reference.

With addressing the SC application, Figs. 2(c) and 2(d) show the optical responses of the designed radiative cooler at sunlight and infrared bands, respectively, where the ideal spectra are plotted for reference. It can be clearly seen that a very good spectral selectivity is obtained at the considered wavelength band (e.g., 0.35−25 μm). Within 0.35−1.1 μm, the radiative cooler functions similarly to the multilayer anti-reflection film. Hence, the radiative cooler obtains the high transmission with average T ~ 0.82, where the average T is 0.90 at the ranges of 0.4−0.9 μm. Within 1.1−4 μm band, the radiative cooler is strongly reflective with average R > 0.91 to eliminate the parasitic heat absorption of SC. The obtained R is higher than the previous work ~ 30%.[21, 22] Simultaneously, the radiative cooler features the near-unity broadband thermal emission at the 4−25 μm band [see Fig. 2(d)], where the average

E reaches 0.92 under transverse-electric (TE) incidence [transverse-magnetic (TM) situation shows similar behavior].

For practical radiative cooling applications, the independences on the incident angle and light polarization are significant. Fig. 3(a) [Fig. 3(b)] plots the emissivity of the radiative cooler versus the incident wavelength and angle for TE (TM) situation. It can be seen that the radiative cooler features a high emissivity at the infrared band even under a very large incident angle (no matter TE or TM incidence has been used). In order to estimate the overall thermal emission performance of the radiative cooler, the spectrally (within the 4−25 μm infrared band) averaged emission characteristics are plotted as the function of the incident angle, as shown in Fig. 3(c) for both TE and TM cases, respectively. Despite of a lower thermal emission at the 4−5 μm band, a high emissivity can be obtained under a

Nanoscale

large range of incident angle. For example, the average emissivity surpasses 0.9 with an incident angle up to 50° for both polarizations; increasing the incident angle to 70°, the average emissivity under the unpolarized incidence [(TE + TM)/2)] can still be over 0.8. Therefore, it is obvious that the emission properties of the radiative cooling SC system are insensitive with the incident angle and light polarization. What is unexpected that the spectral selectivity of radiative cooling GaAs-Si-based and perovskite-Si-based tandem SCs system are similar compared to the Si system, implying that the designed radiative cooler can be applied for various SCs, as exemplified in Fig. 3(d).
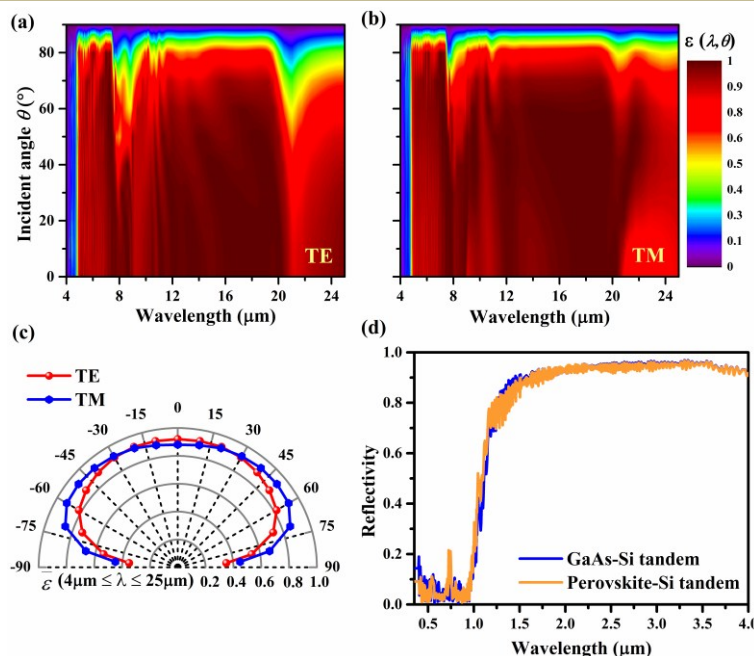
Fig.3 The angle-dependent emissivity spectra of the radiative cooler under (a) TE and (b) TM incidences. (c) The average emissivities of the radiative cooler as functions of polar angle under TE and TM incidences. (d) The reflectivity spectra of the Si-based tandem solar cells.

3.2 Electrical and thermodynamic responses of radiative cooling c-Si SCs

Based on the above structure through the photonic design, a comprehensive OET simulation can be performed, which enables a complete and simultaneous evaluation on both macroscopic and microscopic responses of the system in optical, electrical, and thermodynamic domains. The detailed energy analyses are shown in Fig. 4 and summarized in Table 2. In this calculation, both the temperature of SC and ambient air are chosen to be 300 K under dark condition; moreover, the non-radiative heat exchange coefficients for the top and bottom boundaries of the radiative cooling system are h_{top} = 8 and h_{bottom} = 5 W/m^2/K, respectively.[18, 19] Fig. 4(a) plots the spectra of the power densities reflected back, transmitted through and absorbed by the system. Here, the standard AM 1.5 solar spectrum is given for reference. Moreover, the absorptions by the radiative cooling layers (P_{Abs}^{C}) and the SC (P_{Abs}^{SC}) are distinguished. For the solar incidence, the power density at the silicon band (0.35–1.1 μm) is 800.94 W/m^2 (80.8%); and 189.72 W/m^2 (19.2%) at 1.1–4 μm band (see Table 2). For the designed radiative cooling c-Si SC, the power densities reflected and the absorbed by the radiative cooling layers are only ~ 80.71 W/m^2 (10.1%) and ~ 43.02 W/m^2 (5.4%), respectively, showing the high-performance filtering effect at the c-Si SC band (see Table 2). Consequently, it ensures that the solar energy of 677.21 W/m^2 (84.5%) can reach the SC for electricity generation. Here, a thin-film c-Si SC with Si thickness of 10 μm is used, which shows an absorption power density of 528.91 W/m^2 (66.0%) and a transmitted power density of 148.30 W/m^2 (18.5 %) as shown

in Fig. 4(a). At 1.1–4 μm band, the power density of 159.12 W/m^2 (83.9%) is reflected by the radiative cooler and the c-Si SC does not show noticeable absorption (see Table 2).

The OET simulation also facilitates the evaluation on the electrical and thermal responses under various electrical biases. For example, Fig. 4(b) plots the output power density of the SC and the thermal radiative power density (P_{rad}) of the radiative cooler as functions of the forward electrical bias. For all SCs, the absorbed solar energy can only partly be converted into electricity (P_{PV}), with the remaining being converted into heat (i.e., increasing the SC temperature). Due to the energy conservation, the sum of electricity and heat power should be identical to the absorbed solar energy. The energy conservation obeys the following relation:[4]

$$P_{sun}(x,y,z) = P_{th}(x,y,z) + P_{Joule}(x,y,z) + P_{rec}^{bulk}(x,y,z) + P_{rec}^{surf}(x,y)$$
$$+ P_{Peltier}(x,y) + P_{PV}$$

(15)

where the terms on the right side of the equation are the power densities by the thermalization, Joule heat, bulk recombination, surface recombination, Peltier effect, and SC output, respectively. Therefore, under the short-circuit situation, P_{PV} = 0, implying that the solar power absorbed by the SC is completely dissipated by various heat mechanisms; in this case, the operation temperature of the SC is 328.58 K (55.43 °C). However, at the point with the highest P_{PV}, the dissipated heat in SC reaches the minimum and the operating temperature of SC is decreased to 322.88 K (49.73 °C). For the radiative cooling SC system, the energy difference between absorbed

ARTICLE

energy (including the absorbed solar illumination and atmosphere radiation) and outward energy (the thermal radiation, non-radiative heat exchange and electrical output) has the following conservation:

$$0 = P_{rad}(T) + P_{non}(T, T_{amb}) - P_{sun} + P_{PV} - P_{atm}(T_{amb}) \qquad (16)$$

where P_{non} includes the top and bottom non-radiative heat exchanges (P_{non}^T & P_{non}^B).

Fig. 4(c) demonstrates the thermal radiation spectra of the radiative cooler and the ambient air at the respective temperatures. The blackbody radiations are also used as the reference. Besides, the overall thermal radiation power densities of the radiative cooler and the atmosphere at various bands are labelled. It is shown that our designed cooler has an emission spectrum that is very close to that of the ideal blackbody system under the same temperature. The difference of the radiation power densities between the radiative cooler and the atmosphere directly reflects the radiative cooling effect. As illustrated in Fig. 4(c), at the 8−13 μm band, the radiative cooler shows the strongest cooling effect since 1) the strong thermal

radiation of the cooler occurs at this band and 2) it is the first atmosphere transparency window with a very low radiation from the atmosphere. It should be noted that the second atmosphere window exists at the 16−22 μm band,[39, 40] but the radiative cooling effect is very weak due to the lower thermal emission of the cooler.

The thermodynamic characteristics obtained in the radiative cooling system at the maximum power point of SC are summarized in Fig. 4(d). It can be seen that: 1) for the SC, the solar illumination absorbed by the cell is P_{Abs}^{SC} ~ 528.9 W/m² with a relatively low output power P_{PV} ~ 105.2 W/m² (due to the very thin Si material under consideration), i.e., a large portion is converted into heat (P_{heat}^{SC} ~ 423.7 W/m²); 2) for the radiative cooler, the absorbed solar illumination is only P_{heat}^{C} ~ 63.4 W/m²; 3) the radiative power density absorbed from atmosphere is P_{atm} ~ 238.3 W/m²; 4) the calculated non-radiative power densities at the top (h_{top} = 8 W/m²/K) and bottom (h_{bottom} = 5 W/m²/K) are 182.9 and 111.4 W/m², respectively; 5) the radiative one can reach 428.4 W/m².
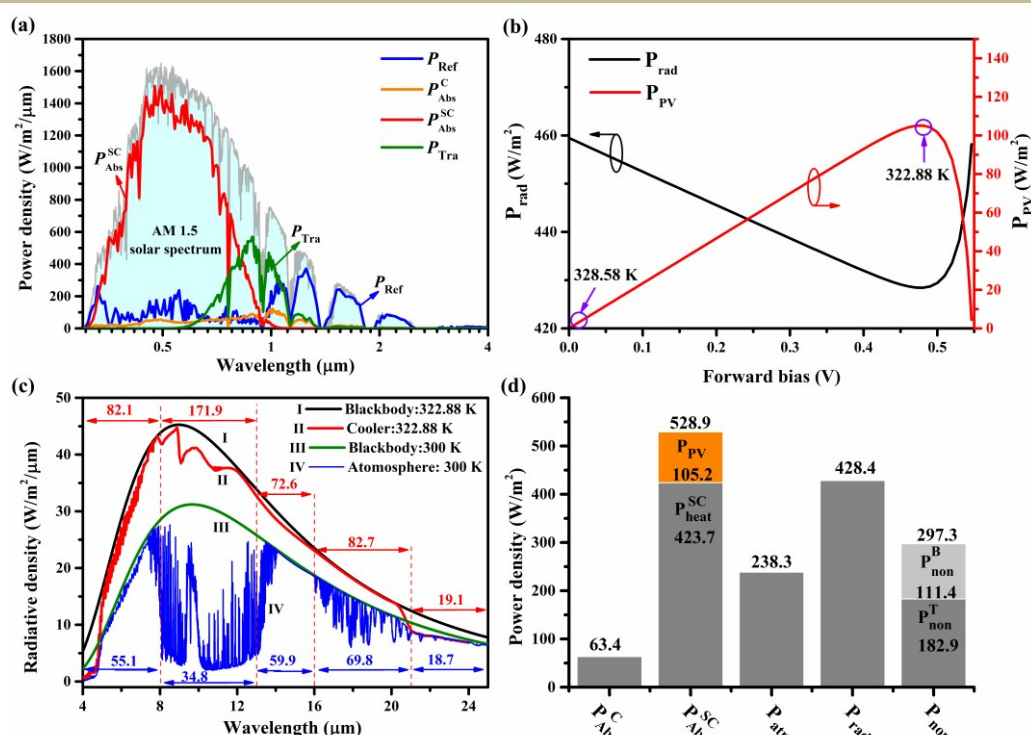

Fig.4 Macroscopic energy analysis of radiative cooling SC system. (a) The power density spectra reflected (blue) and transmitted (green) by the whole radiative cooler, as well as absorbed by radiative cooler (orange) and by SC (red), with standard AM 1.5 solar spectrum for reference. (b) The radiation power density of radiative cooler (P_{rad}) and the electricity output power density of SC (P_{PV}) as functions of the forward bias. (c) The radiative power densities of radiative cooler (P_{rad}) and atmosphere emission power density (P_{atm}) distribution as functions of radiation wavelength. (d) The quantitative analysis of power density components within the radiative cooling SC system at the maximum power point of SC.

Table 2 Macroscopic energy analysis of the radiative cooling SC system.

Solar spectrum (W/m²)	P_{Ref}	P_{Abs}^{C}	P_{Abs}^{SC}	P_{Tra}
0.35−1.1 (μm)	800.94	80.71	43.02	528.91	148.30
	(80.8%)	(10.1%)	(5.4%)	(66.0%)	(18.5%)
1.1−4 (μm)	189.72	159.12	14.89	0.002	15.71
	(19.2%)	(83.9%)	(7.8%)	(0.0%)	(8.3%)
Total			990.66		

Since the SC is a coupled OET system, the carrier thermodynamic characteristics are closely related with the carrier

transport behaviors. Figs. 5(a) and 5(b) quantitatively analyze the bias-dependent carrier electrodynamic and thermodynamic

characteristics, respectively. Under a low forward electrical bias (e.g., 0–0.41 V), the built-in electric field is weakened, but without qualitatively affecting the carrier-separation capability; thus, J_{sc} is almost unchanged as shown in Fig. 5(a). Correspondingly, Fig. 5(b) shows that under such a low bias: 1) the Joule heat is gradually declined due to the weakened built-in electric field; 2) P_U and $P_{Peltier}$ remain unchanged with the increase of forward bias; and 3) P_{th} is independent of the bias since it only relies on the band-gap of SC material. By contrast, under a large forward bias (e.g., 0.42–0.54 V), the carrier cannot be effectively transported over the p-n junction, leading to the higher carrier recombination. It is observed that all of the top, bottom and bulk recombination current densities (J^T_{surf}, J^B_{surf} and J_{bulk}) are rapidly increased as displayed in Fig. 5(a), leading to much higher recombination heat (P_U) in Fig. 5(b). In addition, the pie chart of the current density components at maximum power point is inserted in Fig. 5(a), which indicates that 87.6% of the photocurrent

is collected by the electrode, and J^T_{surf} and J^B_{surf} are the main recombination-induced photocurrent losses in SC. Besides, the quantitative analysis of thermodynamic behaviors at the maximum power point of SC are summarized in Table 3. It can be seen that: 1) the absorbed power density of 47.05% (248.87 W/m²) is lost by the thermalization, which can be significantly reduced by using the tandem SC structure; 2) the energy of 83.20 W/m² is lost by Joule heat; and 3) the power densities consumed by the recombination and Peltier heats are 34.75 and 56.93 W/m², respectively. For the recombination heat in the SC, it can be effectively reduced by optimizing the carrier transportation process (e.g., tailoring doping concentration, energy band alignment and surface passivation strategy) of SC. [5–7, 27, 28] As well as, the Peltier heats can be greatly reduced by diminishing the interface barrier between SC and metal-electrode (e.g., regulating the work function of metal-electrode).[4]
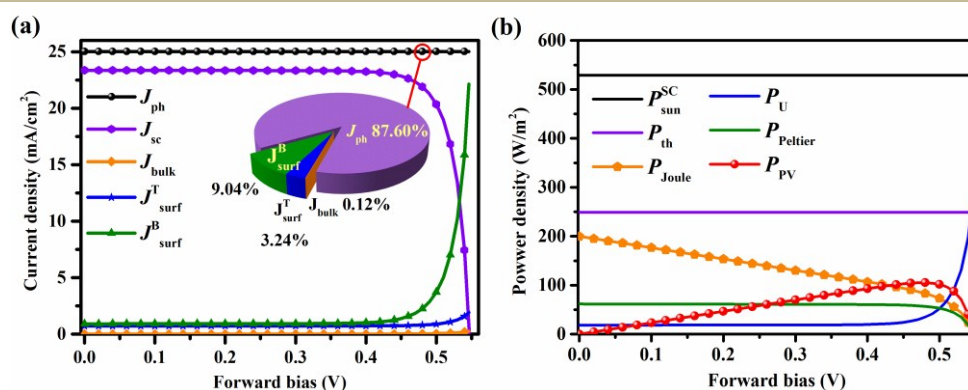

Fig.5 The microscopic quantitative analysis obtained in SC. (a) The carrier electrodynamics behaviors, with the pie chart of current density components at maximum power point inserted. (b) The carrier thermodynamics behaviors versus the forward electrical bias.

Table 3 Microscopic energy analysis of carrier thermodynamics at the maximum power point of SC.

Thermodynamic channels	Thermal	Joule	Recombination	Peltier	Electricity
Power density (W/m²)	248.87 (47.05%)	83.20 (15.73%)	34.75 (6.57%)	56.93 (10.76%)	105.16 (19.88%)

3.3 Comparable study on radiative cooling c-Si SCs

We would like to have a comparable study on the thermal characteristics of the considered thin-film c-Si SC with and without the radiative cooler design. For fairness, the comparable study is based on two conditions: 1) the SCs under both situations absorb the sunlight identically, and 2) the same non-radiative heat exchange coefficients (h_{top} = 8 W/m²/K at the top and h_{bottom} = 5 W/m²/K at the bottom) are selected. In fact, through our OET simulation, the steady-state temperature distribution inside the SC can be obtained, which can well reflect how the radiative cooler affects the thermal response of the SC. Plotted in Fig. 6(a) are the spatial temperature distributions of the SCs without [(a1)] and with [(a2)] the cooler. It is obvious that the temperature gradient in the SC only is ~ 0.001 °C due to the high thermal conductivity (130 W/m/K) of Si material;[41] moreover, there are slight lateral variations of the temperature due to the introduction of the grating layer in the radiative cooling part. For the bare SC, the cell temperature is be heated up to ~ 332.94 K (59.79 °C) from environmental 300 K due to the sunlight illumination, as shown in Fig. 6(a1). However, with the incorporation of radiative cooler, the cell temperature is lowed to 322.88 K (49.73 °C), i.e., a temperature drop of over 10 °C, as shown in Fig. 6(a2).

We further examine how the radiative cooler improves the photoconversion performance of the SC. The current-voltage (J-V) curves of the SCs before and after employing the radiative cooler are plotted in Fig. 6(b), where the short-circuit current density (J_{sc}), open-circuit voltage (V_{oc}), fill factor (FF), and PCE (η) can all be obtained and compared. With increasing the operation temperature of the SC, J_{sc} can be affected through: 1) the equilibrium carrier population increases exponentially, leading to a higher dark current density and lower J_{sc};[42] 2) the temperature gradient exited in SC can provide a thermal diffusion force for the carrier to form a thermal current density, which is beneficial for the increase of J_{sc}. Eventually, the thermal current density outweighs the dark saturation current density and a relatively higher J_{sc} can be obtained for the bare SC without the radiative cooler [Fig. 6(b)]. However, the value of V_{oc} exponentially reduces with the increase of the dark current at the higher temperature and leads to the obvious decrease of V_{oc}.[42] Fig. 6(b) shows that V_{oc} decreases by about 2.1 mV/°C, which agrees well with the experiments.[43] Therefore, the net temperature effect is the reduction of PCE of SC with increasing the operating temperature, which reveals that the incorporation of radiative cooler can be useful for sustaining a high PCE. This can be seen from Fig. 6(b) that the PCE of the SC can be increased by 0.43% after employing the radiative cooler.

ARTICLE

In practice, the non-radiative effects can also lower the operating temperature of SC,[13] estimated by the non-radiative heat exchange coefficient ($h_c = h_{top} + h_{bottom}$), which remarkably affects the radiative cooling effect. Hence, the temperature decline (ΔT) of SC after employing the radiative cooler and the P_{rad} of radiative cooler

as the functions of h_c are explored in Fig. 6(c). It can be observed that the operating temperature of SC can be cooled by over 23 °C with h_c = 8 W/m²/K;[18, 29] even for a large h_c = 15 W/m²/K,[18] the temperature deduction of ~ 8 °C and a considerably high P_{rad} over 415 W/m² can still be achieved.
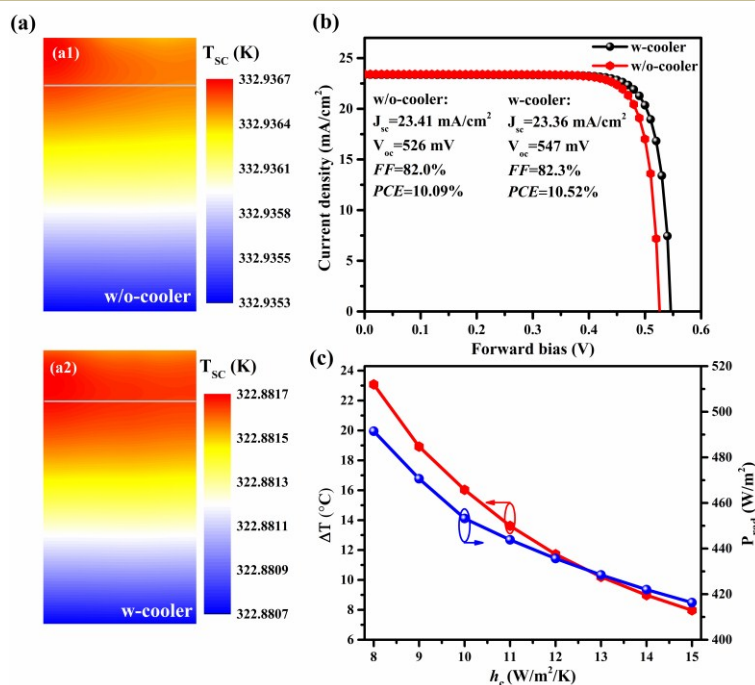
Fig.6 (a) The temperature distribution within the SC under the sunlight illumination, where (a1) and (a2) are for the cases without and with radiative cooler, respectively. (b) The temperature effect on the current-voltage (*J-V*) characteristics of SC without and with radiative cooler, where the key performance parameters J_{sc}, V_{oc}, FF and PCE are inserted. (c) The temperature deduction of SC (ΔT) and radiation power density as functions of h_c.

Finally, considering the actual environmental situation in a day, the time-dependent performance of the radiative cooling SC is
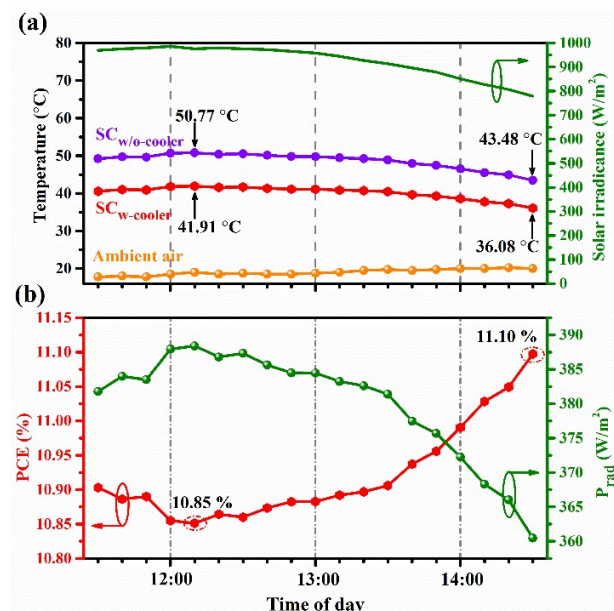
Fig.7 (a) Operating temperatures of the c-Si SCs without/with the radiative cooler with the change of weather condition in a day, where the solar irradiance and ambient temperature are selected from the actual environment situation with h_c = 13 W/m²/K. (b) The corresponding variations of the PCE of SC and the radiation power density of the radiative cooler with the time from 11:30–14:30.

studied. Combining the experimental data of solar irradiance and ambient air temperature.[18] Fig. 7 demonstrates the variations of the temperature and PCE of the SC as well as the radiative power density of the radiative cooler versus the time of a day. In the time range within 11:30–14:30, the solar irradiance gradually declines while the temperature of ambient air is rising with time. Near the peak of solar irradiance, the SC reaches the highest temperature of ~ 50.77 °C (41.91 °C) under bare (radiative cooler) design, demonstrating that the SC temperature can be cooled by 8.86 °C. With the solar irradiance getting weaker, the SC temperature shows a rapid decline. At the time of 14:30, the SC temperatures are 43.48 °C and 36.08 °C for the bare and radiative cooling SCs, respectively, i.e., temperature decline by radiative cooler is 7.4 °C. In addition, the PCE of the SC and the radiative power density of the cooler are sensitive to the operating temperature as shown in Fig. 7(b). The radiative power density over 360 W/m² can be obtained even with a relative lower operating temperature (e.g., 36.08 °C).

4 Conclusions

In summary, we realized the comprehensive multi-dimensional OET simulation of photonic radiative coolers with concerning the applications in reliable high-efficiency photovoltaic cells. Especially, the fundamental physical mechanisms of the radiative cooling SC systems are quantitatively analyzed from the macroscopic and microscopic perspectives by addressing the optical, electrical and thermal effects simultaneously. We proposed a photonic radiative cooler with the near-ideal

Journal Name

ARTICLE

spectral selectivity from the sunlight to infrared band, which features the angle, polarization-independence properties. Based on the OET model, we presented a detailed analysis of macroscopic energy conversion processes (including the absorbed solar illumination, radiative powwer of radiative cooler and atmosphere, non-radiative heat exchange, the output power of electricity and net-cooling cooling power) in radiative cooling SC system. Besides, the coupled carrier electrodynamic (carrier generation/recombination/transportation/collection) and thermodynamic (thermalization, Joule, recombination and Peltier heat) behaviors in SC were quantitatively evaluated under the forward bias. Further, the fundamental mechanisms that temperature effect on the performance (J_{sc}, V_{oc}, FF, η) of SC are explored. Our results demonstrated that the absolute efficiency of SC increases by ~ 0.43% and the SC operating temperature declines by ~ 10.16 °C can be performed after employing the designed radiative cooler. The temperature effect significantly restricts the voltage of the SC, and the high performance SC can be implemented by integration with photonic radiative cooler. Our comprehensive OET study provides a readily way to explore the intrinsic OET physics of photovoltaic and other OET-related optoelectronic systems. It can also effectively guide the design of reliable and high-performance OET devices.

## Conflicts of interest

There are no conflicts to declare.

Acknowledgements

References

1   W. Shockley, H. J. Queisser, *J. Appl. Phys.*, 1961, **32**, 510.
2   U. Lindefelt, *J. Appl. Phys.*, 1994, **75**, 942.
3   J. E. Parrott, *IEEE Trans. Electron. Dev.*, 1996, 43, 809.
4   A. Shang, X. Li, *Adv. Mater*., 2017, **29**, 1603492.
5   K. Yoshikawa, H. Kawasaki, W. Yoshida, T. Irie, K. Konishi, K. Nakano, T. Uto, D. Adachi, M. Kanematsu, H. Uzu, K. Yamamoto, *Nat. Energy*, 2017, **2**, 17032.
6   G. J. Bauhuis, P. Mulder, E. J. Haverkamp, J. C. C. M. Huijben, J. J. Schermer, *Sol. Energ. Mat. Sol. C.*, 2009, **93**, 1488.
7   N. J. Jeon, H. Na, E. H. Jung, T. Y. Yang, Y. G. Lee, G. Kim, H. W. Shin, S. I. Seok, J. Lee, J. Seo, *Nat. Energy*, 2018, **3**, 682.
8   G. Tamizh Mani, L. Ji, Y. Tang, L. Petacci, C. Osterwald, *NCPV and Solar Program Review Meeting*, March 2003, Denver, CO, USA.
9   X. Sun, T. J. Silverman, Z. Zhou, M. R. Khan, P. Bermel, M. A. Alam, *IEEE J. Photovolt.*, 2017, **7**, 566.
10 E. Skoplaki, J. A. Palyvos, *Sol. Energy*, 2009, **83**, 614.
11 S. Kurtz, K. Whitfield, G. TamizhMani, M. Koehl, D. Miller, J. Joyce, J. Wohlgemuth, N. Bosco, M. Kempe, T. Zgonena, *Prog. Photovolt: Res. Appl.*, 2011, **19**, 954.
12 X. Zhang, X. Zhao, J. Shen, J. Xu, X. Yu, *Appl. Energ.*, 2014, **114**, 335.
13 R. Mazon-Hernandez, J. R. Garcia-Cascales, F. Vera-Garcia, A. S. Kaiser, B. Zamora, *Int. J. Photoenergy*, 2013, **2013**.
14 G. Fraisse, C. Menezo, K. Johannes, *Sol. Energy*, 2007, **81**, 1426.
15 S. D. Sharma, H. Kitano, K. Sagara, *Res. Rep. Fac. Eng. Mie Univ*, 2004, **29**, 31.
16 J. Sieckera, K. Kusakanaa, B. P. Numbib, Renew. Sust. *Energ. Rev.*, 2017, **79**, 192.
17 Y. Lu, Z. Chen, L. Ai, X. Zhang, J. Zhang, J. Li, W. Wang, R. Tan, N. Dai, W. Song, *Sol. RRL*, 2017, **1**, 1700084.
18 L. Zhu, A. P. Raman, S. Fan, *P. Natl. Acad. Sci. USA*, 2015, **112**, 12282.
19 L. Zhu, A. Raman, K. X. Wang, M. A. Anoma, S. Fan, *Optica*, 2014, **1**, 32.
20 Z. Zhou, X. Sun, P. Bermel, *Inter. Soc. Opt. Photon.*, 2016, **9973**, 997308.
21 W. Li, Y. Shi, K. Chen, L. Zhu, S. Fan, *ACS Photonics*, 2017, **4**, 774.
22 B. Zhao, M. Hu, X. Ao, Q. Xuan, G. Pei, *Sol. Energ. Mat. Sol. C.*, 2018, **178**, 266.
23 X. Li, N. P. Hylton, V. Giannini, K. H. Lee, J. Ekins-Daukes, S. A. Maier, *Opt. Express*, 2011, **19**, A888.
24 X. Li, N. P. Hylton, V. Giannini, K. H. Lee, N. J. Ekins-Daukes, S. A. Maier, *Prog. Photovolt: Res. Appl.*, 2013, **21**, 109.
25 A. Shang, X. Zhai, C. Zhang, Y. Zhan, S. Wu, X. Li, *Prog. Photovolt: Res. Appl.*, 2015, **23**, 1734.
26 L. Chen, S. Wu, D. Ma, A. Shang, X. Li, *Nano Energy*, 2018, **43**, 177.
27 Y. An, A. Shang, G. Cao, S. Wu, D. Ma, X. Li, *Sol. RRL*, 2018, **2**, 1800126.
28 A. Shang, Y. An, D. Ma, X. Li, *AIP Adv.*, 2017, **7**, 085019.
29 A. P. Raman, M. A. Anoma, L. Zhu, E. Rephaeli, S. Fan, *Nature* 2014, **515**, 540.
30 IR Transmission Spectra, Gemini Observatory, https://www.gemini.edu/sciops/telescopes-and-sites/observing-condition-constraints/ir-transmission-spectra.
31 E. W. Peterson, Jr. J. P. Hennessey, *J. Appl. Meteorol. Clim.*, 1978, **17**, 390.
32 Y. Shi, W. Li, A. Raman, S. Fan, *ACS Photonics*, 2018, **5**, 684.
33 Y. Zhai, Y. Ma, S. N. David, D. Zhao, R. Lou, G. Tan, R. Yang, X. Yin, *Science* 2017, **355**, 1062.
34 E. Rephaeli, A. Raman, S. Fan, *Nano Lett.*, 2013, **13**, 1457.
35 Z. Chen, L. Zhu, A. R. S. Fan, *Nat. Commun.*, 2016, **7**, 13729.
36 D. Zhao, A. Aili, Y. Zhai, J. Lu, D. Kidd, G. Tan, X. Yin, *Joule*, 2018, **3**, 1.
37 J. Kischkat, S. Peters, B. Gruska, M. Semtsiv, M. Chashnikova, M. Klinkmüller, O. Fedosenko, S. Machulik, A. Aleksandrova, G. Monastyrskyi, Y. Flores, W. T. Masselink, *Appl. Opt.*, 2012, **51**, 6789.
38 E. D. Palik, *Handbook of Optical Constants of Solids*, 1st ed. Academic Press: San Diego, CA, 1997.
39 X. Sun, Y. Sun, Z. Zhou, M. A. Alam, P. Bermel, *Nanophotonics*, 2017, **6**, 997.
40 C. G. Granqvist, A. Hjortsberg, J. Appl. Phys., 1981, **52**, 4205.
41 M. Levinshtein, S. Rumyantsev, M. Shur, *Handbook series on semiconductor parameters*, Vol. 1. World Scientific, Singapore, 1996.
42 J. Nelson, *The physics of solar cells*, World Scientific, London, 2003.
43 M. A. Green, *Solar cells: operating principles, technology, and system applications*, Prentice-Hall, Inc., Englewood Cliffs, 1982.

TOC Graphic:
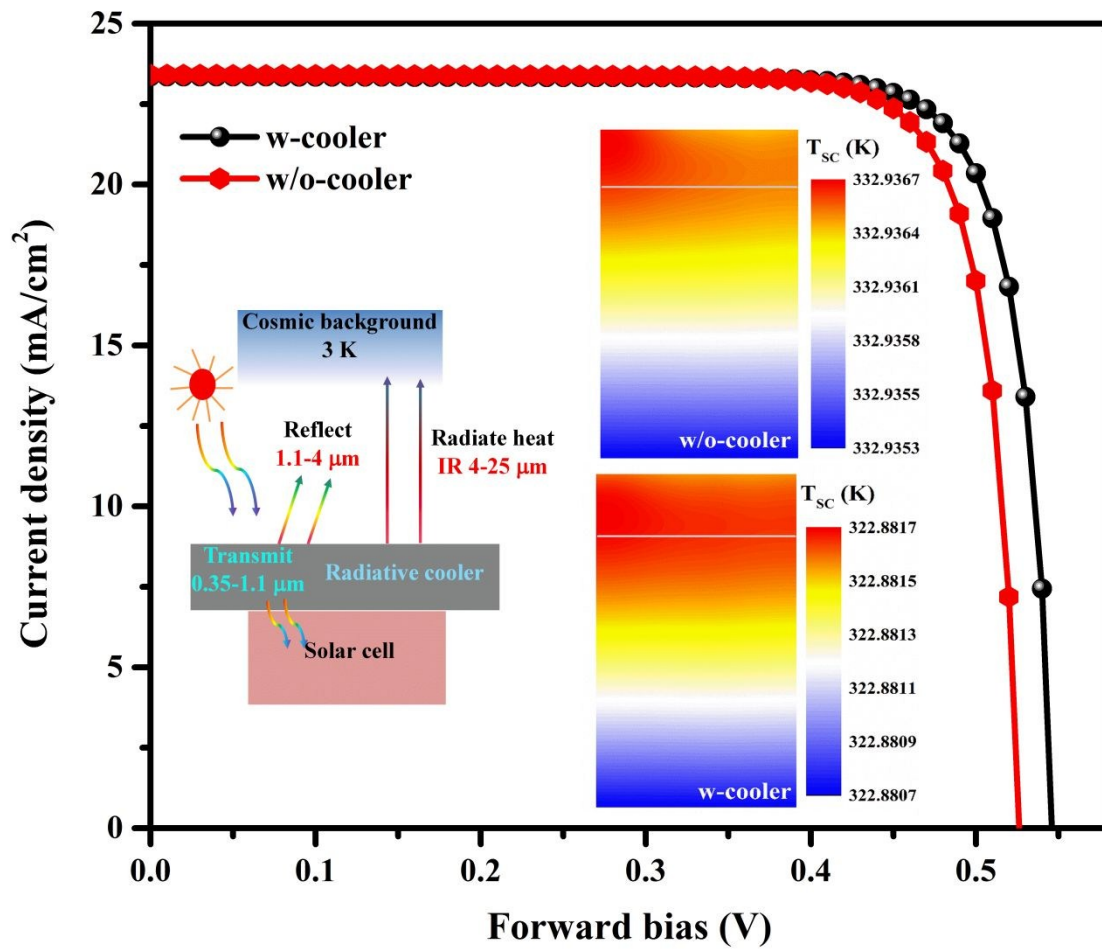
The comprehensive multi-dimensional opto-electro-thermal (OET) modeling of radiative cooling solar cell (SC) system and the temperature effect on the performance of SC